Complex Analysis of Askaryan Radiation: UHE-ν Identification and Reconstruction using the Hilbert Envelope of Observed Signals

Jordan C. Hanson[*] and Raymond Hartig

Department of Physics and Astronomy, Whittier College

(Dated: February 6, 2026)

The detection of ultra-high energy neutrinos (UHE-ν), with enegies above 10 PeV, has been a long-time goal in astroparticle physics. Autonomous, radio-frequency (RF) UHE-ν detetectors have been deployed in polar regions that rely on the Askaryan effect in ice for the neutrino signal. The Askaryan effect occurs when the excess negative charge within a UHE-ν cascade radiates in a dense medium. UHE-ν can induce cascades that radiate in the RF bandwidth above thermal backgrounds. To identify UHE-ν signals in data from Askaryan-class detectors, analytic models of the Askaryan electromagnetic field have been created and matched to simulations and laboratory measurements. These models describe the Askaryan electromagnetic field, but leave the effects of signal propagation through polar ice and RF channel response to simulations. In this work, a fully analytic Askaryan model that accounts for these effects is presented. First, formulas for the observed voltage trace and its Hilbert envelope are calculated. Second, the analytic model is compared to UHE-ν signals at 100 PeV from NuRadioMC, a key Monte Carlo toolset in the field. Correlation coefficients between the analytic signal envelope and MC data in excess of 0.94 are found, and 99.99% of UHE-ν signals pass a correlation threshold of $\rho \geq 0.4$. Analysis of RF thermal noise reveals that just 0.2 background events have $\rho \geq 0.4$ in 5 years at a 1 Hz thermal trigger rate. Finally, we describe future work related to the measurement of the logarithm of the UHE-ν cascade energy.

Keywords: Ultra-high energy neutrino; Askaryan radiation; Mathematical physics

I. INTRODUCTION

Cosmic neutrinos with energies up to 100 PeV have been detected by the IceCube and KM3NeT collaborations [1–8]. Previous analyses indicate that the discovery of UHE-ν flux above 5 PeV requires large Askaryan-class detectors [9]. UHE-ν could reveal the source of ultra-high energy cosmic rays (see sections 3.1-3.3 of [10]). Further, studying electroweak interactions at these energies is impossible on Earth, and Askaryan-class neutrino detectors will provide new data (see section 3.4 of [10]).

J. C. Hanson and R. Hartig presented the first fully analytic model of the Askaryan field in the time-domain (HH2022) [11]. The model builds on earlier work from J. C. Hanson and A. L. Connolly (JCH+AC), who developed an analytic form factor for the instantaneous charge distribution (ICD) that explains the low-pass filtering of the Askaryan spectrum, and cascade elongation from the LPM effect [12]. When correlated against semi-analytic parameterizations used in NuRadioMC (AHRZ2020), which involve numeric convolution of UHE-ν cascade data with an analytic vector potential, the HH2022 model yields correlation coefficients in excess of 0.95 [11, 13]. Hanson and Hartig listed three advantages of analytic models in HH2022: measuring cascade parameters from the fit of analytic model to observed waveforms, minimization of computational intensity in NuRadioMC, and the potential to embed analytic models on-board detectors to reject thermal noise in real time.

Though the fully anaytic approach in HH2022 allowed precise reconstruction of UHE-ν cascade parameters, it was limited to comparisons between the simulated and theoretical $\vec{E}$-fields. Askaryan-class detectors actually observe voltage traces that represent the RF detection channel response, convolved with $\vec{E}$-fields that have propagated through kilometers of polar ice. NuRadioMC accounts for these effects by incorporating measurements from years of lab and field work [14–25]. In this work, we present the first fully analytic Askaryan model in the time-domain that matches the observed voltage traces.

In practice, it is common to compute the Hilbert envelope of voltage traces from RF channels before cross-correlating them. This is done to remove oscillations introduced by the RF antennas in the channels, which can confuse cross-channel timing and reconstruction. Our calculations include both the voltage trace, and the Hilbert envelope of the trace. The work is organized as follows. Units, definitions, and notational conventions are given in Sec. II. The calculations of the observed voltage trace and Hilbert envelope of the trace are given in Sec. III. These results are compared to NuRadioMC output in Sec. IV. In Sec. V, a preliminary reconstruction of the logarithm of the cascade energy from the UHE-ν interaction is given. The key findings are summarized in Sec. VI.

II. UNITS, DEFINITIONS, AND CONVENTIONS

The analysis is based on two analytic functions: the Askaryan signal, $s(t)$, and the RF channel response, $r(t)$. The RF detection channel is a linear, time-invariant DSP system. Thus, the observed voltage trace in an Askaryan-

Variable	Definition	Units
c	speed of light in medium	m ns^{-1}
r	distance to cascade peak	m
t_r	$t - r/c$	ns
θ_C	Cherenkov angle	radians
θ	viewing angle from cascade axis	radians
a	longitudinal cascade length (see [26])	m
n_{max}	max excess cascade particles (see [26])	none
E_0	$\propto n_{max} a$ (see [26])	V GHz^{-2}
p	$\frac{1}{2}(a/c)^2 (\cos\theta - \cos\theta_C)^2$ (see [11])	ns^2
ω_0	$\sqrt{\frac{2}{3}}(c\sqrt{2\pi}\rho_0)/(\sin\theta)$ (see [12])	GHz
$\sqrt{2\pi}\rho_0$	lateral ICD width (see [12])	m^{-1}

TABLE I: Parameters relevant for Eq. 3.

class detector is the convolution of $r(t)$ and $s(t)$, $r(t) * s(t)$. Let $\hat{s}(t)$ represent the Hilbert transform of $s(t)$, and let $j = \sqrt{-1}$. The *analytic signal*, $s_a(t)$, and *signal envelope*, $\mathcal{E}_s(t)$, are defined by

$$s_a(t) = s(t) + j\hat{s}(t) \quad (1)$$
$$\mathcal{E}_s(t) = |s_a(t)| \quad (2)$$

The signal envelope actually observed by Askaryan-class detectors is the envelope of $r(t) * s(t)$, written as $\mathcal{E}_{r*s}(t)$. The result for $\mathcal{E}_{r*s}(t)$ depends on the model for $s(t)$, taken to be Eq. 28 in HH2022 [11]:

$$r\vec{E}(t_r, \theta) = -\frac{E_0 \omega_0 \sin(\theta)}{8\pi p} t_r e^{-\frac{t_r^2}{4p} + p\omega_0^2} \operatorname{erfc}(\sqrt{p}\omega_0) \quad (3)$$

The parameters of Eq. 3 are shown in Tab. I. Though Ralston and Buniy (RB) [26] used c for the vacuum value of the speed of light, the formulae for $r\vec{E}$ presented in [26] refer to the wavenumber k in the medium, which is proptional to the index of refraction. Thus, the use of c in this work refers to the speed of light in the medium. For example, a phase factor of $\exp(jkr)$ could also be written $\exp(jr\omega/c)$, if c refers to the value in the medium. The distance r is between the observer and the radiating charge at the cascade peak. The longitudinal length over which $\Delta r < \lambda$, the RF wavelength in ice, is named the *coherence zone* Δz_{coh} in the RB model. The Δz_{coh} is limited by what RB call the "acceleration argument," that $r(t)$ is accelerating while keeping $\Delta r < \lambda$.

The time t is the independent variable of the inverse Fourier transform of the equations in [26]. The delayed time is $t_r = t - r/c$. The speed c is equal to the vacuum value, divided by the index of refraction n. For RF in ice, $n = 1.78$. The viewing angle θ is the zenith angle in spherical coordinates, if the cascade axis is the z-axis. The Cherenkov angle is $\cos\theta_C = 1/n$ for relativistic cascades, and for the RF bandwidth in ice, $\theta_C = 55.8$ degrees. The longitudinal cascade length, a, is set by

the cascade physics. The ratio $\eta = (a/\Delta z_{coh})^2$ corresponds to the far-field limit as $\eta \to 0$, but $\eta \to 0$ is not a requirement. JCH+AC found that η corresponds to a low-pass filter for the RF spectrum with cutoff frequency ω_C: $\eta = \omega/\omega_C$ [12].

The n_{max} parameter is the maximum number of excess negative cascade charges, and the overall RF amplitude, E_0, is propotional to $n_{max} a$ [26]. JCH+AC and HH2022 demonstrated that the frequency ω_0 is related to the ICD and the cascade form factor [11, 12]. Monte Carlo simulations have shown that the lateral dependence of the ICD is exponentially distributed [12, 27]. JCH+AC derived the form factor by modeling the lateral component of the ICD as an exponential distribution, which in turn makes the form factor act as a low-pass filter with cutoff ω_0. Finally, the authors of HH2022 showed that p in Tab. I is related to σ_t, the pulse width of $s(t)$ [11]:

$$\sigma_t = \sqrt{2p} \quad (4)$$

The authors of HH2022 have shown that, because $\cos\theta - \cos\theta_C \approx -\sin\theta_C(\theta - \theta_C)$ to first order in $\Delta\theta = (\theta - \theta_C)$, $p \propto \Delta\theta^2$ to second order, and

$$a\Delta\theta = \frac{c\sigma_t}{\sin\theta_C} \quad (5)$$

Qualitatively, this notion was identified by RB in Sec. III of [26]. The authors of HH2022 analyzed the relationship between a, the cascade energy E_C and the critical energy E_{crit} for electromagnetic and hadronic cascades [11]. Let $E_C/E_{crit} = \Lambda$. Assuming the Greisen and Gaisser-Hillas parameterizaions for electromagnetic and hadronic cascades, respectively, the following relationships for the a-values from electromagentically dominated and hadronically dominated cascades were found:

$$a_{em} = x_{em}\sqrt{\ln\Lambda} \quad (6)$$
$$a_{had} = x_{had}\sqrt{\ln\Lambda} \quad (7)$$

The values for x_{em} and x_{had} are calculated in Sec. V. From Eq. 5, the fractional error in $\ln\Lambda$ is:

$$\frac{\sigma_{\ln\Lambda}}{\ln\Lambda} = 2\left(\frac{\sigma_a}{a}\right) \quad (8)$$

Equation 8 corresponds to Eq. 42 in [11], and has been corrected for units. Equations 4-8 imply measurements of a and $\Delta\theta$ yield $\ln\Lambda$, and that the relative error in $\ln\Lambda$ is proportional to the relative error in a.

III. CALCULATION OF THE MAIN RESULTS

The parameters in Eq. 3 that do not depend on time can be folded into a single constant, E_0, leaving only the

time-dependence. From now on, let t refer to t_r, without the subscript. The signal model $s(t)$ is

$$s(t) = -E_0 t e^{-\frac{1}{2}(t/\sigma_t)^2} \qquad (9)$$

This is the *off-cone* equation from [11]. The parameter σ_t is the pulse width, and it depends two quantities: a and $\Delta\theta$ (Eq. 5). The parameter E_0 is the amplitude normalization, and the dependencies on other parameters can be determined from Eq. 3 and Tab. I. The most important of these is the $1/r$ dependence (Eq. 3). To achieve the goal of $\mathcal{E}_{r*s}(t)$, the Hilbert transform and analytic signal of $s(t)$ are required. The Hilbert transform $\widehat{s}(t)$ is equivalent to the convolution of $s(t)$ and the tempered distribution $h(t) = 1/(\pi t)$. The implication in the Fourier domain is that the negative frequencies in the spectrum of $\hat{s}(t)$ vanish, while the positive ones are doubled. Let the sgn(f) be -1 if $f < 0$, 0 if $f = 0$, and 1 if $f > 1$, and let $S(f)$ be the Fourier transform of $s(t)$. The Fourier transform of the analytic signal $s_a(t)$ is

$$\mathcal{F}\{s_a(t)\}_f = S_a(f) = S(f)(1 + \text{sgn}\, f) \qquad (10)$$

Thus, if $f < 0$, $S_a(f) = 0$, and $S_a(f) = 2S(f)$ if $f \geq 0$. Taking the inverse Fourier transform of Eq. 10, the analytic signal may be written in terms of $S(f)$:

$$s_a(t) = 2 \int_0^\infty S(f) e^{2\pi j f t} df \qquad (11)$$

The Fourier transform of Eq. 9 is

$$S(f) = E_0 \sigma_t^3 (2\pi)^{3/2} j f e^{-2\pi^2 f^2 \sigma_t^2} \qquad (12)$$

Using the gaussian spectral width σ_f from [12], and the guassian width of $s(t)$ from [11], it was shown in [11] that the uncertainty principle holds for off-cone signals:

$$\sigma_t \sigma_f \geq \frac{1}{2\pi} \qquad (13)$$

The equality is reached in the limit the far-field parameter limits to zero: $\eta \to 0$. This makes the signal spectrum

$$S(f) = E_0 \sigma_t^3 (2\pi)^{3/2} j f e^{-\frac{1}{2}(f/\sigma_f)^2} \qquad (14)$$

Inserting $S(f)$ into Eq. 11, $s_a(t)$ is

$$s_a(t) = \frac{E_0 \sigma_t^3 (2\pi)^{3/2}}{\pi} \frac{d}{dt} \int_0^\infty e^{-\frac{1}{2}(f/\sigma_f)^2} e^{2\pi j f t} df \qquad (15)$$

Let $k^2/4 = \frac{1}{2}(f/\sigma_f)^2$, and $x = t/(\sqrt{2}\sigma_t)$. Equation 15 can be broken into real and imaginary parts:

$$s_a(t) = \frac{E_0 \sigma_t}{\sqrt{2\pi}} \frac{dI}{dx} \qquad (16)$$

$$\Re\{I\} = \int_0^\infty e^{-k^2/4} \cos(kx) dk \qquad (17)$$

$$\Im\{I\} = \int_0^\infty e^{-k^2/4} \sin(kx) dk \qquad (18)$$

The real part of I is even, so it can be extended to $(-\infty, \infty)$ if it is multiplied by $1/2$. The result is

$$\Re\{I\} = \sqrt{\pi} e^{-x^2} \qquad (19)$$

The imaginary part of I is proportional to the *Dawson function*, $D(x)$ [28]:

$$\Im\{I\} = 2D(x) \qquad (20)$$

The overall analytic signal, $s_a(t)$, is

$$s_a(t) = -E_0 \left(t e^{-\frac{1}{2}(t/\sigma_t)^2} - \frac{2j\sigma_t}{\sqrt{2\pi}} \frac{dD(x)}{dx} \right) \qquad (21)$$

The envelope of the signal, $\mathcal{E}_s(t)$, is the magnitude of Eq. 21. Though $D(x)$ is not evaluated analytically, a high-precision algorithm for computing $D(x)$ was given in [29]. As expected, $|s_a(0)| \neq 0$, since $dD(x)/dx = 1 - 2xD(x)$.

The observed data in Askaryan-class detectors is the convolution of the UHE-ν signal from the ice and the detector response function. To generate *signal templates*, Askaryan radiation signals are calculated for the UHE-ν interaction properties, modified by the frequency-dependent RF attenuation of polar ice, and convolved with the RF channel response [14, 15]. Signal templates are cross-correlated with observed data to identify UHE-ν signals. RF detection channels based on RF dipole antennas, however, have resonance frequencies that introduce oscillations not present in the original signal. The oscillations can introduce timing uncertainties. The problem intensifies when the signal-to-noise ratio (SNR) relative to RF thermal noise decreases.

To reduce uncertainties, the Hilbert envelope of observed data is used in cross-correlations instead of the original signals. Thus, an analytic prediction for the Hilbert envelope of the observed data would an effective signal template. An assumption must be made, however, for the RF channel response, $r(t)$. The RLC impulse response was first used by RICE at the South Pole at a model for RF dipole channels [30]. The RLC damped oscillator is a suitable circuit model for the RF dipole channels for two reasons. First, dipoles respond within a bandwidth centered around a resonance frequency, just as RLC circuits do. Second, RF dipole channels are used in RICE, ARA, RNO-G, and the proposed IceCube Gen2 because these channels must fit inside cylindrical ice boreholes [10, 30–33]. Thus, the model chosen for $r(t)$ is the damped oscillation of an RLC circuit.

There are two paths to calculating the final result, $\mathcal{E}_{r*s}(t)$. The first involves three steps. First, the detector response, $r(t)$ is convolved with $s(t)$. Second, the analytic signal of the result is found. Third, the magnitude of the analytic signal is computed, which can be compared to envelopes of observed signals. The second path involves computing $\mathcal{E}_{r*s}(t)$ directly from $s_a(t)$ and $r_a(t)$. The second option is more straightforward, once a special theorem relating $r_a(t)$, $s_a(t)$, and $\mathcal{E}_{r*s}(t)$ is established. $\mathcal{E}_{s*r}(t)$, $s_a(t)$, and $r_a(t)$ are related by

$$\mathcal{E}_{s*r}(t) = \frac{1}{2}|s_a(t) * r_a(t)| \qquad (22)$$

The proof of Eq. 22 is based on two ideas. First, the Hilbert transform of a function $s(t)$ is equivalent to convolving it with $h(t) = 1/(\pi t)$. Second, the Hilbert transform is an *anti-involution*, meaning acting it twice on a function $f(t)$ yields $-f(t)$: $h * h * f = -f$. Given the definitions of $s_a(t)$ and $\hat{s}(t)$,

$$(s * r)_a(t) = s * r + j\,\widehat{s * r} \qquad (23)$$

$$\mathcal{E}_{s*r}(t) = |s * r + js * r * h| \qquad (24)$$

However,

$$r_a * s_a = (r + j\hat{r}) * (s + j\hat{s}) \qquad (25)$$

$$r_a * s_a = r * s + jr * \hat{s} + j\hat{r} * s - \hat{r} * \hat{s} \qquad (26)$$

$$r_a * s_a = r * s - r * h * s * h + 2jh * r * s \qquad (27)$$

$$r_a * s_a = r * s - h * h * r * s + 2jh * r * s \qquad (28)$$

$$r_a * s_a = 2r * s + 2jh * r * s \qquad (29)$$

Multiplying both sides $1/2$ and taking the magnitude completes the proof:

$$\frac{1}{2}|r_a * s_a| = |r * s + jh * r * s| = \mathcal{E}_{s*r}(t) \qquad (30)$$

Assume that a signal arrives in an RLC damped oscillator at $t = 0$. For $t \geq 0$, the impulse response and corresponding analytic signal are

$$r(t) = R_0 e^{-2\pi\gamma t} \cos(2\pi f_0 t) \qquad (31)$$

$$r_a(t) = R_0 e^{-2\pi\gamma t} e^{2\pi j f_0 t} \qquad (32)$$

The parameters γ and f_0 are the decay constant and the resonance frequency. Note that the envelope of $r(t)$, $|r_a(t)|$, is $R_0 \exp(-2\pi\gamma t)$, as expected. To prove Eq. 32, first compute the Fourier transform of $r(t)$:

$$R(f) = \frac{R_0}{4\pi j}\left(\frac{1}{f - z_+} + \frac{1}{1 - z_-}\right) \qquad (33)$$

$$z_+ = f_0 + j\gamma \qquad (34)$$

$$z_- = -f_0 + j\gamma \qquad (35)$$

Given Eq. 11, the procedure to find $r_a(t)$ is to multiply the *negative* frequency component at z_- by 0 and the *positive* frequency component at z_+ by 2, and take the inverse Fourier transform. The inverse Fourier transform may be completed by applying Jordan's lemma in the complex plane frequency plane. The residue from the pole at z_+ yields the result.

The goal is now to apply Eq. 22 by convolving $s_a(t)$ with $r_a(t)$. The calculation may be split into two parts: $r_a(t) * \Re\{s_a(t)\}$, and $r_a(t) * \Im\{s_a(t)\}$. Let $u(t)$ represent the Heaviside step function. Starting with $r_a(t) * \Re\{s_a(t)\}$:

$$r_a(t) * \Re\{s_a(t)\} =$$
$$R_0 e^{2\pi j f_0 t} e^{-2\pi\gamma t} u(t) * \left(-E_0 t e^{-\frac{1}{2}(t/\sigma_t)^2}\right) \qquad (36)$$

Let $x = t/(\sqrt{2}\sigma_t)$, $y = \tau/(\sqrt{2}\sigma_t)$, and $z = (2\pi j f_0 - 2\pi\gamma)\sqrt{2}\sigma_t$. Changing variables while accounting for the relationship between $u(t)$, x, and y, gives

$$r_a(t) * \Re\{s_a(t)\} =$$
$$-2R_0 E_0 \sigma_t^2 \int_{-\infty}^{x} e^{z(x-y)} y e^{-y^2} dy \qquad (37)$$

Note that the units for the convolution of $r(t)$ and $s(t)$ are $R_0 E_0 \sigma_t^2$. Let $u = x - y$, so that $du = -dy$. The result is

$$r_a(t) * \Re\{s_a(t)\} = 2R_0 E_0 \sigma_t^2 \left(\frac{dI(x,z)}{dz} - xI(x,z)\right) \qquad (38)$$

where

$$I(x,z) = \int_0^{\infty} e^{zu} e^{-(u-x)^2} du \qquad (39)$$

Let $b = x + \frac{1}{2}z$. Completing the square in the exponent and substituting $k = u - b$ gives

$$I(x,z) = e^{-x^2} e^{b^2} \int_{-b}^{\infty} e^{-k^2} dk$$
$$= \frac{\sqrt{\pi}}{2} e^{-x^2} e^{b^2} \operatorname{erfc}(-b) \qquad (40)$$

Let $b = jq$, and $w(q)$ be the *Faddeeva function* [28]. The integral becomes

$$I(x,z) = \frac{\sqrt{\pi}}{2} e^{-x^2} w(q) \qquad (41)$$

The chain rule is required to find dI/dz:

$$\frac{dI}{dz} = \frac{dI}{dq}\frac{dq}{dz} = -\left(\frac{j}{2}\right)\frac{dI}{dq} \qquad (42)$$

The final result is

$$r_a(t) * \Re\{s_a(t)\} =$$
$$-\sqrt{\pi} R_0 E_0 \sigma_t^2 \left(x e^{-x^2} w(q) + \left(\frac{j}{2}\right) e^{-x^2} \frac{dw(q)}{dq}\right) \qquad (43)$$

Turning to the convolution of $r_a(t)$ with $\Im(s_a)$,

$$r_a(t) * \Im\{s_a(t)\} =$$
$$\left(R_0 e^{2\pi j f_0 t} e^{-2\pi\gamma t} u(t)\right) * \left(\frac{2E_0 \sigma_t^2}{\sqrt{\pi}} \frac{dD(t/\sqrt{2}\sigma_t)}{dt}\right) \qquad (44)$$

Note that $f'(t) * g(t) = f(t) * g'(t) = (f(t) * g(t))'$. Thus,

$$r_a(t) * \Im\{s_a(t)\} =$$
$$\frac{2}{\sqrt{\pi}} R_0 E_0 \sigma_t^2 \frac{d}{dt}\left(e^{2\pi j f_0 t} e^{-2\pi\gamma t} u(t) * D(t/\sqrt{2}\sigma_t)\right) \qquad (45)$$

The convolution becomes

$$r_a(t) * \Im\{s_a(t)\} =$$
$$\frac{2}{\sqrt{\pi}} R_0 E_0 \sigma_t^2 \frac{d}{dt} \int_{-\infty}^{t} e^{(2\pi j f_0 - 2\pi\gamma)(t-\tau)} D(\tau/\sqrt{2}\sigma_t) d\tau \quad (46)$$

Adopting the earlier definitions of x, y, and z gives

$$r_a(t) * \Im\{s_a(t)\} =$$
$$\frac{2}{\sqrt{\pi}} R_0 E_0 \sigma_t^2 \frac{d}{dx} \int_{-\infty}^{x} e^{z(x-y)} D(y) dy \quad (47)$$

Using Leibniz rule for the fundamental theorem of calculus, and the limiting cases of $D(x)$,

$$r_a(t) * \Im\{s_a(t)\} =$$
$$\frac{2}{\sqrt{\pi}} R_0 E_0 \sigma_t^2 \left(D(x) + z \int_{-\infty}^{x} e^{z(x-y)} D(y) dy \right) \quad (48)$$

Let $u = x - y$, $z = -k$, and note that $D(x)$ is an odd function. These substitutions give

$$r_a(t) * \Im\{s_a(t)\} =$$
$$\frac{2}{\sqrt{\pi}} R_0 E_0 \sigma_t^2 \left(D(x) + k \int_{0}^{\infty} e^{-ku} D(u - x) du \right) \quad (49)$$

The remaining integral is the Laplace transform of the shifted Dawson function, $\mathcal{L}\{D(u-x)\}_k$. The final result is

$$r_a(t) * \Im\{s_a(t)\} =$$
$$\frac{2}{\sqrt{\pi}} R_0 E_0 \sigma_t^2 \left(D(x) + k\mathcal{L}\{D(u-x)\}_k \right) \quad (50)$$

Though a closed analytic form for $\mathcal{L}\{D(u-x)\}_k$ is elusive, evaluating $\mathcal{L}\{D(u-x)\}_k$ numerically is fast and precise. A short code that demonstrates how this Laplace transform is computed is given in Appendix A.

Combining Eq. 43 and Eq. 50 gives $r_a(t) * s_a(t)$:

$$r_a(t) * s_a(t) =$$
$$- \sqrt{\pi} R_0 E_0 \sigma_t^2 \left(xe^{-x^2} w(q) + \left(\frac{j}{2}\right) e^{-x^2} \frac{dw(q)}{dq} \right) +$$
$$\frac{2j}{\sqrt{\pi}} R_0 E_0 \sigma_t^2 \left(D(x) + k\mathcal{L}\{D(u-x)\}_k \right) \quad (51)$$

The units of convolution should be $R_0 E_0 \sigma_t^2$, and each term in Eq. 51 has these units. Remember that the relationship between q and x is given by

$$q = -jb = -j\left(x + \frac{z}{2}\right) \quad (52)$$

Taking the magnitude of Eq. 51, and multiplying by $1/2$, yields the **Hilbert envelope of the convolution of $s(t)$ with $r(t)$:**

$$\mathcal{E}_{r*s}(t) = \frac{1}{2}|r_a(t) * s_a(t)| \quad (53)$$

To model the full time-dependent voltage trace from detection channels, and not merely the envelope, $s(t) * r(t)$ is required. The calculation may be done analytically, starting with the definition of convolution:

$$s(t) * r(t) = \int_{-\infty}^{\infty} s(t-\tau)r(\tau)d\tau \quad (54)$$

As in the calculation of $\mathcal{E}_{r*s}(t)$, the Heaviside step function, $u(t)$ is included to ensure causality. Inserting the definitions of $s(t)$, $r(t)$, and $u(t)$ gives

$$s * r =$$
$$-E_0 R_0 \int_{-\infty}^{\infty} (t-\tau) e^{-\frac{1}{2}\left(\frac{t-\tau}{\sigma_t}\right)^2} \Re\left\{e^{2\pi j f_0 \tau} e^{-2\pi\gamma\tau}\right\} u(\tau)d\tau$$
$$(55)$$

Using the previous definitions of x, y, and z gives

$$s * r = -2R_0 E_0 \sigma_t^2 \int_{0}^{\infty} (x-y) e^{-(x-y)^2} \Re\left\{e^{zy}\right\} dy \quad (56)$$

Note that the $\Re\{\}$ operator can encompass the whole integral, since $s(t)$ is real. Splitting the integral and employing differentiation under the equals sign yields

$$s * r =$$
$$- 2R_0 E_0 \sigma_t^2 \Re\left\{ xe^{-x^2} I(x,z) - \frac{1}{2} e^{-x^2} \frac{dI(x,z)}{dx} \right\} \quad (57)$$

with

$$I(x,z) = \int_{0}^{\infty} e^{-y^2+(2x+z)y} dy \quad (58)$$

Let $b = x + \frac{1}{2}z$, and $b = jq$. The calculation resembles that of $r_a(t) * \Re\{s_a(t)\}$. The result for $I(x,z)$ is

$$I(x,z) = \frac{\sqrt{\pi}}{2} w(q) \quad (59)$$

Inserting this result into Eq. 57, gives

$$s * r = -\sqrt{\pi} R_0 E_0 \sigma_t^2$$
$$\Re\left\{ xe^{-x^2} w(q) - \frac{1}{2} e^{-x^2} \frac{dw(q)}{dx} \right\} \quad (60)$$

From the definition of q and the chain rule, $dw(q)/dx = -jdw(q)/dq$, and $dw(q)/dq = -2qw(q) + 2j/\sqrt{\pi}$ [28]. The final result is left in terms of $\Re\{w(q)\}$ and $\Re\{-jdw(q)/dq\}$, which are proportional to the *Voigt functions* [11, 28].

$$s * r = -\sqrt{\pi} R_0 E_0 \sigma_t^2$$
$$\left(xe^{-x^2} \Re\{w(q)\} - \frac{1}{2} e^{-x^2} \Re\left\{ -j\frac{dw(q)}{dq} \right\} \right) \quad (61)$$

To illustrate the accuracy of the model, the *numerically-computed envelope* of Eq. 61 is compared to Eqs. 51-53 in Fig. 1. The *numerical convolution* of $s(t)$ and $r(t)$ is compared to Eq. 61 in Fig. 2.
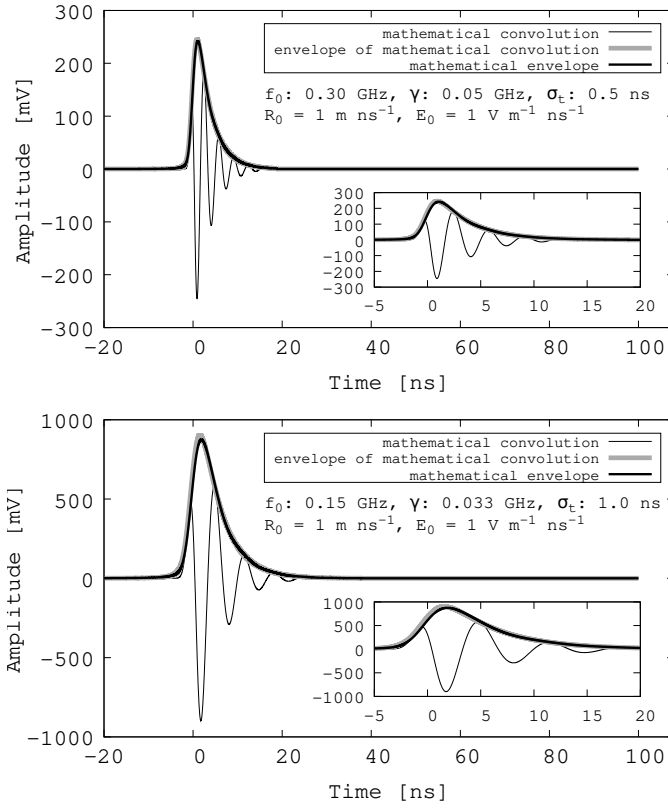
FIG. 1: (Top) The thin black line represents $s*r$ from Eq. 61. The gray envelope represents the envelope of Eq. 61 computed with the Python3 SciPy function scipy.special.hilbert. The black envelope represents $\mathcal{E}_{r*s}(t)$ from Eqs. 51-53. (Bottom) Same as top, different parameters.
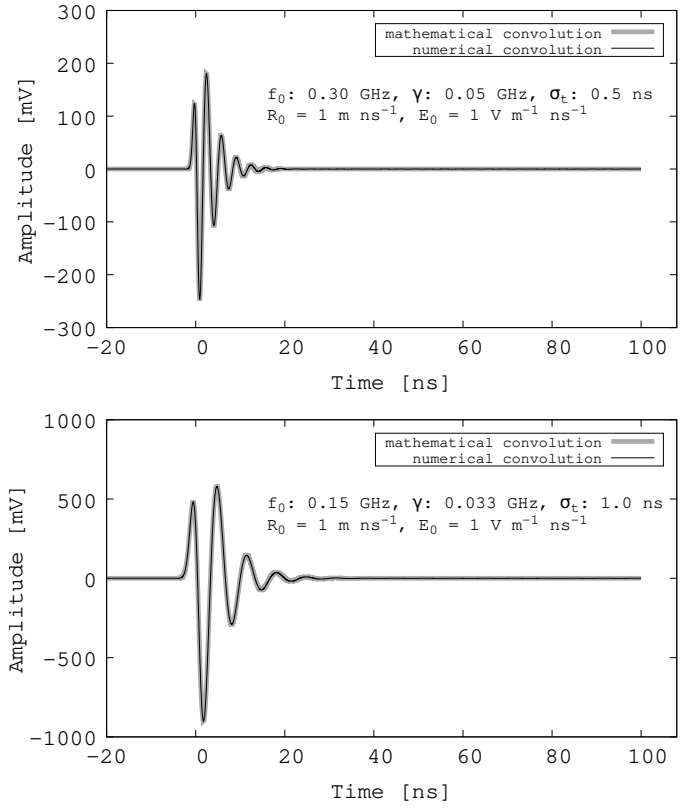
FIG. 2: (Top) The thin black line represents $s(t)$ from Eq. 9 convolved with $r(t)$ from Eq. 31, using the Python3 SciPy function scipy.signal.convolve. The gray line represents $s*r$ from Eq. 61. (Bottom) Same as top, different parameters.

IV. COMPARISON BETWEEN ANALYTIC CALCULATIONS AND NURADIOMC

NuRadioMC was used to generate UHE-ν interactions in a cylindrical ice volume (see Tab. II). The 100 PeV interactions included charged and neutral electroweak currents, and the LPM effect. The Askaryan model used in NuRadioMC was AHRZ2020 [13]. AHRZ2020 is a *semi-analytic* parameterization of the Askaryan effect, in which a vector potential $\vec{A}(\vec{r}, t)$ is convolved with the profile of the net charge in the UHE-ν cascade. AHRZ2020 accounts for sub-cascades and the LPM effect, and it has been validated against MC simulations [27, 34]. The Askaryan model used in NuRadioMC for this analysis was *not* HH2022, so correlations between MC output and Eqs. 51-53 are solely on physical grounds.

The detector was *a single string* of 8 RF dipoles, each with the same (x,y)-coordinates and regularly-spaced z-coordinates. The ice had a depth and radius of 0.65 km and 0.85 km, respectively, and the accounted for measurements of the attenuation length versus frequency collected from the South Pole region [32, 35]. Each RF channel had a filtered, amplified passband of [0.08-1] GHz, 256 samples, and a 1 GHz sampling rate. The RF trigger responded when any 3 of the 8 voltage traces exceeded $+3$ times *and* -3 times the rms voltage (v_{rms}) of the thermal noise within 256 ns (256 samples). The rms voltage, v_{rms}, is characterized in NuRadioMC via the *noise temperature*, which was set to 233 K.

The Hilbert envelope of the coherently summed waveform (CSW) was calculated from the traces and cross-correlated with Eqs. 51-53, producing correlation coefficients. Each coefficient was maximized by varying only σ_t. The RF channel properties, f_0 and γ, were held constant. To find the optimal f_0 and γ, the noise temperature was set to 3 K, so that thermal noise was negligible. The values for f_0 and γ that yielded optimal correlation cofficients were 0.15 GHz and 0.025 GHz, respectively. The cross-correlation results are shown in Fig. 3.

In Fig. 3, the circles represent the normalized histogram of the correlation coefficient between the optimized analytic envelope and thermal noise. A fitting function of the form $x^2 \exp(-0.5x^2)$ was fit to the noise distribution, and is represented by the gray dashed line. The solid gray line represents the signal distribution, which peaks at a correlation value of 0.94. Lower signal correlation values correspond to lower SNR values (Fig. 4). The vertical black dashed line represents a threshold of 0.4. For the simulated UHE-ν, 99.99% of correlations

| Parameter	Value	Note
Ice Model	South Pole	2015 measurements
Signal Model	AHRZ2020	(see [13])
Trigger	3 of 8 channels	$\pm 3 v_{\mathrm{rms}}$
RF channels	8	RF bicone (in firn)
Channel filters	[80-1000] MHz	Passband
Noise Temperature	233K	Sets v_{rms}
Sampling Rate	1 GHz	$f_c = 500$ MHz
Samples per channel	256	total time, 256 ns
Channel depths	[-4,-6,-8,...-18] m	cable delays included
RF cable type	LMR-400	≈ -1 dB at 20 m

TABLE II: Important NuRadioMC parameters.
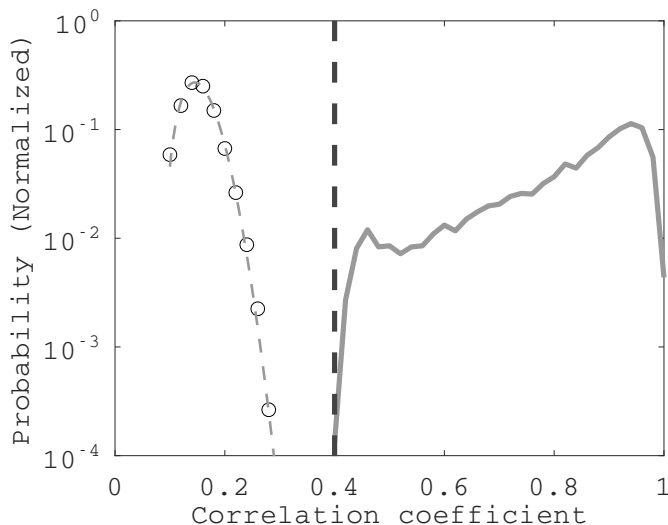
FIG. 3: (Black circles) Noise distribution. (Gray dashed line) Fitting function to noise distribution. (Solid gray line) UHE-ν signal distribution. (Dashed black line) Correlation threshold.

exceed this threshold. Assuming a thermal trigger rate of 1 Hz, integrating the PDF of the noise distribution above the correlation threshold is equivalent to 0.2 noise events every 5 years. An example CSW fit by the analytic envelope is shown in Fig. 5.

To ensure this result is interpretable, we studied the effect of our NuRadioMC trigger threshold on the thermal trigger rate. The *in-situ* stations of ARIANNA, ARA, and RNO-G all use majority logic or phased array triggers that record thermal noise events [36–38]. Individual channels must satisfy the majority logic within a specified gate time. When a thermal noise fluctuation satisfies the majority logic, the system records data, and a dead-time is required to reset the data acquisition system.

We created a computational tool to estimate the thermal trigger rate. With a majority logic of 3 of 8, a dead-time of 10 ms, a gate time of 200 ns (the default setting in NuRadioMC), sampling rate of 1 GHz, and thresholds of $\approx \pm 3.5 v_{\mathrm{rms}}$, we found that Gaussian white noise triggered at ≈ 1 Hz. The difference between thresholds
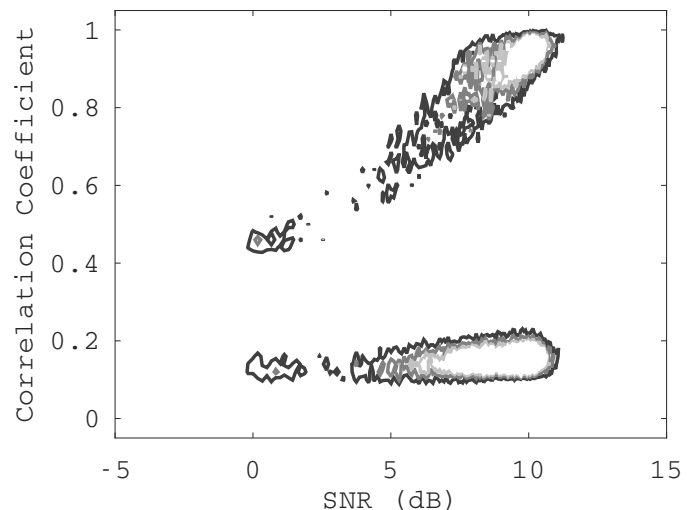
FIG. 4: The correlation versus SNR (dB) for UHE-ν signals (upper distribution) and RF thermal noise (lower distribution). Color scale: normalized histogram value, with five equally spaced contours between 0.0 and 0.002.
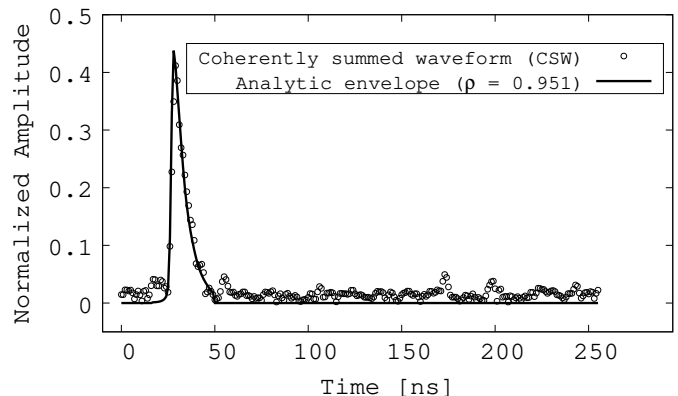
FIG. 5: A single-pulse CSW signal (black dots) from a 100 PeV UHE-ν, matched to an analytic envelope (thick black line) with a correlation coefficient $\rho = 0.951$.

of $\pm 3.5 v_{\mathrm{rms}}$ and $\approx \pm 3.0 v_{\mathrm{rms}}$ is negligible for fitting Eqs. 51-53 to CSWs from UHE-ν events. Though we found that such thermal trigger rates allow just 0.2 thermal noise events to pass the correlation threshold in 5 years, this result can be scaled to the appropriate thermal rate, given the details in [36–38].

The correlation between the optimized analytical envelope and UHE-ν signals depends on the SNR (dB). Let v_{pp} represent the peak-to-peak value in the voltage trace. The SNR (dB) is

$$\mathrm{SNR}_{\mathrm{dB}} = 20 \log_{10} \left(\frac{1}{2} \frac{v_{\mathrm{pp}}}{v_{\mathrm{rms}}} \right) \qquad (62)$$

In Fig. 4, the correlation coefficient is plotted versus the SNR in dB for the data shown in Fig. 3. The upper

and lower distributions correspond to CSWs from UHE-ν events and thermal noise, respectively. All RF thermal noise events satisfy the station trigger. Note that the correlation coefficient for UHE-ν events is proportional to SNR_{dB}. The SNR of a CSW does not equal the SNR of the individual voltage traces. Rather, the voltage traces will have SNRs 5-9 dB *lower* than the CSW. If N voltage traces contain signal, computing the CSW raises the linear SNR by a factor of $\sqrt{N}$, and adds $10\log_{10}(N)$ to SNR_{dB}. For an event with 3 of 8 channels containing signal, $10\log_{10}(3) \approx 5$ dB, while $10\log_{10}(8) \approx 9$ dB.

Our technique has may be applied in a variety of ways. Though we compared CSWs to Eqs. 51-53 for this analysis, Eqs. 51-53 can also be matched to individual RF channels. Future work could include a nuanced analysis that only includes RF channels in the CSW that meet a SNR_{dB} criteria. Further, our technique applies to all types of RF dipole channels. (The specific one used in our analysis is in Tab. II). The only requirement for the RF channel is that $r(t)$ from Sec. III represents a good model of the impulse response, and that suitable values for f_0 and γ can be measured. An important use case is to model the RF phased-array channels of RNO-G [38]. In the seven deployed stations, the RF dipole channels are located at depths that ensure the index of refraction is constant, meaning $r(t)$ should serve at least as well as it did for the RF channels of the RICE detector [30].

V. MEASUREMENT OF $\log_{10} E_{\text{C}}$

In the following analysis, we summarize a technique that yields a measurement of the logarithm of the UHE-ν cascade energy, $\ln \Lambda$, using Eqs. 5-8. For Eq. 5, σ_t is measured from the optimized analytic envelope, c and θ_{C} are known constants. The $\Delta\theta$ must be measured separately from σ_t, or assumption must be made about its value. Suppose that $\Delta\theta$ is distributed normally, with zero mean, so that $\Delta\theta \approx \Delta\theta_{\text{rms}}$. Solving Eq. 5 for a gives

$$a = \frac{c\sigma_t}{\Delta\theta_{\text{rms}} \sin\theta_{\text{C}}} \quad (63)$$

The result for the fractional error in a is found by propagating error from σ_t and $\Delta\theta$, defined as ϵ and $\sigma_{\Delta\theta}$, respectively. The result is

$$\frac{\sigma_a}{a} = \left(\left(\frac{\epsilon}{\sigma_t}\right)^2 + \left(\frac{\sigma_{\Delta\theta}}{\Delta\theta}\right)^2 \right)^{1/2} \quad (64)$$

The first term is small compared to the second, as it is limited by the scan resolution for σ_t and the number of samples per analytic envelope. In Sec. IV, the scan resolution was set to 0.2 ns. There are typically > 10 samples per envelope, or about 10 ns. The fractional error in $\Delta\theta$ would be 1.0, because the rms and σ values are equal for

normal distributions with zero mean. Thus, $(\epsilon/\sigma_t)^2$ is two orders of magnitude smaller than $(\sigma_{\Delta\theta}/\Delta\theta)^2$, so

$$\frac{\sigma_a}{a} = \left|\frac{\sigma_{\Delta\theta}}{\Delta\theta}\right| = \left|\frac{\Delta\theta_{\text{rms}}}{\Delta\theta_{\text{rms}}}\right| \approx 1 \quad (65)$$

Inserting $(\sigma_a/a) \approx 1$ into Eq. 8 gives

$$\frac{\sigma_{\ln\Lambda}}{\ln\Lambda} \approx 2 \quad (66)$$

Using Eqs. 6 and 7, the logarithm of the energy is

$$\ln\Lambda = \left(\frac{c\sigma_t}{x_{\text{em/had}}\Delta\theta_{\text{rms}} \sin\theta_{\text{C}}}\right)^2 \quad (67)$$

Using Eqs. 10 and 12 from HH2022 ([11]), x_{em} and x_{had} were found to be 0.80 and 0.93 meters, respectively (FWHM, $R = 0.5$). Using Eq. 67, the σ_t results from the optimized envelope fits to UHE-ν signals could be used to deduce the logarithm of the UHE-ν cascade, $\log_{10} E_{\text{C}}$. First, converting to the base-10 logarithm introduces a factor of $\ln(10)$ in the denominator of Eq. 67. Second, $\ln\Lambda = \ln(E_{\text{C}}/E_{\text{crit}})$, where E_{C} is the cascade energy, and $E_{\text{crit}} \approx 10^8$ eV is known as the critical energy [11]. Since $\ln\Lambda = \ln E_{\text{C}} - \ln E_{\text{crit}}$, separating this ratio adds $\log_{10} E_{\text{crit}}$ to the right hand side of Eq. 67. Third, let x_{ave} be the average of x_{em} and x_{had}, to reflect the unknown cascade type. The modified form of Eq. 67 is

$$\log_{10} E_{\text{C}} = \frac{(c\sigma_t)^2}{\ln 10 (x_{\text{ave}}\Delta\theta_{\text{rms}} \sin\theta_{\text{C}})^2} + \log_{10} E_{\text{crit}} \quad (68)$$

In hopes of using Eq. 68 to measure $\log_{10} E_{\text{C}}$, we calculated the σ_t distribution derived from 15133 UHE-ν events that triggered the detector with $E_{\text{C}} = 100$ PeV. Though the σ_t distribution corresponds to the correlation coefficient distribution in Fig. 3, two effects conspire to cause the measurement of $\log_{10} E_{\text{C}}$ to break down. First, the dependence of $\log_{10} E_{\text{C}}$ in Eq. 68 on σ_t is *quadratic*, so subtle shifts in σ_t amplify error in $\log_{10} E_{\text{C}}$. Second, *reflected signals* lead to extended tails in the σ_t distribution that skew measurements of the average of $\log_{10} E_{\text{C}}$.

Reflected signals occur within traces either when signals from two ray-tracing paths are available, or when part of the signal reflects from the surface back to the RF channel. Signals that propagate directly to the detector are known as *direct signals*, while signals that reflect at the snow-air interface are known as *reflected signals*. Complex RF signal propagation in polar ice has been studied, and even proposed as a UHE-ν energy reconstruction technique [21, 24, 39].

When reflected signals are present in the CSW, the fitting algorithm compensates with unphysical σ_t values corresponding to a single pulse (see Fig. 6). This compensation leads to an overestimation of $\log_{10} E_{\text{C}}$. To account for reflected signals, we would have to assume two
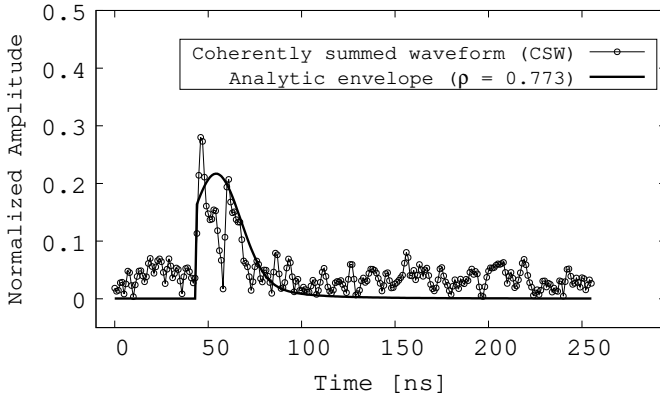
FIG. 6: A CSW signal with a reflection (black dots and thin black line) from a 100 PeV UHE-ν, matched to an analytic envelope (thick black line), with $\rho = 0.773$.

independent copies of Eqs. 51-61 for each UHE-ν event, and scan for two σ_t values and two pulse locations within the waveform. Though not conceptually difficult, we felt the technique was beyond the scope of this work.

VI. CONCLUSION

In Secs. I and II, previous work in the utility of analytic Askaryan models was reviewed, and important parameters were defined. In Sec. III, a fully analytic model for $\mathcal{E}_{\mathrm{s}*\mathrm{r}}(t)$ and $s(t) * r(t)$ was presented and checked for accuracy. In Sec. IV, the analytic model was shown to reject all but 0.2 RF thermal triggers in a 5 year run at a 1 Hz thermal trigger rate using a correlation threshold of $\rho \geq 0.4$. The threshold $\rho \geq 0.4$ preserves 99.99% of UHE-ν signals at 100 PeV. The correlation distribution for UHE-ν signals peaked at 0.94, and some values even exceed 0.94. Finally, in Sec. V, we sketched a technique to calculate the average $\log_{10} E_{\mathrm{C}}$ from data from a *single-string detector*. The technique breaks down without explicitly accounting for signal reflections.

There are three logical steps for this work in the future. First, we must account for reflected signals when fitting analytic envelopes to CSWs from UHE-ν. The authors of [39] have shown how direct and reflected (DnR) signals may be used to constrain the UHE-ν energy. This procedure should be combined with the analytic envelope fit to advance UHE-ν energy reconstruction. Though this is not difficult, it was beyond the scope of this work.

Second, a separate fit for $\Delta\theta$ should be included. This parameter may be constrained by using the spectral cut-off of the voltage traces, which are inversely correlated to $\Delta\theta$ [12]. With a separate fit for $\Delta\theta$, the a-value could be constrained without making any assumption about $\Delta\theta$. This step would improve the precision of the a-value by lowering the fractional error in a-values in Eq. 64. This procedure was completed in [11], but it is restricted to comparisons between $\vec{E}$-fields and not observed CSWs.

Third, it is interesting to note that the model in this work relies on the *off-cone* ($\theta \neq \theta_{\mathrm{C}}$) version of $s(t)$. The authors of HH2022 [11] also include an *on-cone* version of $s(t)$ that is used when $\Delta\theta = 0$, and can be used as $\Delta\theta \to 0$. The on-cone model could provide a better fit between $\mathcal{E}_{\mathrm{s}*\mathrm{r}}(t)$ for events with $\Delta\theta \lesssim 1$ degree [11]. Further, the on-cone model is defined in a piecewise fashion by rising and falling exponential functions, simplifying the procedure used to arrive at Eqs. 51-53.

Appendix A: Python3 Code for $\mathcal{L}\{D(u-x)\}_k$

The code in this section computes the Laplace transform of the shifted Dawson function, $\mathcal{L}\{D(u-x)\}_k$. The syntax has been adjusted to fit in two-column format, so please check the alignment.

```python
import numpy as np
from scipy.integrate import quad
from scipy.special import dawsn as D
...
def shifted_laplace_transform(self,f,s,t0,t_max=1000):
    x = s.real
    y = s.imag
    re_int = quad(lambda t:
        np.exp(-x*t)*np.cos(y*t)*f(t-t0),0,t_max)[0]
    im_int = quad(lambda t:
        np.exp(-x*t)*np.sin(y*t)*f(t-t0),0,t_max)[0]
    return complex(re_int,-im_int)
...
x = t/(sigma_t*np.sqrt(2))
z = (2*np.pi*J*f0-2*np.pi*gamma)*np.sqrt(2)*sigma_t
k=-z
... + k*self.shifted_laplace_transform(D,k,x))
```

Appendix B: Python3 Example Code for $\mathcal{E}_{\mathrm{s}*\mathrm{r}}(t)$

The code in this section computes $\mathcal{E}_{\mathrm{s}*\mathrm{r}}(t)$. The syntax has been adjusted to fit in two-column format, so please check the alignment.

```python
import numpy as np
from scipy.integrate import quad
from scipy.special import wofz as w
from scipy.special import dawsn as D
...
def shifted_laplace_transform(...):
```

```
...
def dwdq(q):
    J = complex(0,1)
    return 2*J/np.sqrt(np.pi)-2*q*w(q)
def math_env(self,t,E0,R0,sigma_t,f0,gamma):
    units = R0*E0*sigma_t*sigma_t
    J = complex(0,1)
    x = t/(sigma_t*np.sqrt(2))
    z = (2*np.pi*J*f0-2*np.pi*gamma)
    z *= np.sqrt(2)*sigma_t
    k=-z
    q = -J*(x+z/2)
    first = -np.sqrt(np.pi)*(x*np.exp(-x*x)*w(q)
        +0.5*J*np.exp(-x*x)*self.dwdq(q))
    second = 2/np.sqrt(np.pi)*(D(x)
        +k*self.shifted_laplace_transform(D,k,x))
    if(np.isinf(first) or np.isinf(second)
        or np.isnan(first) or np.isnan(second)):
        return 0.0
    else:
        result = units*(first+J*second)
    return 0.5*np.abs(result)
```

Appendix C: Python3 Example Code for $s(t) * r(t)$

The code in this section contains the definitions of $s(t)$ and $r(t)$, and computes $s(t) * r(t)$. The syntax has been adjusted to fit in two-column format, so please check the alignment.

```
import numpy as np
```

```
from scipy.special import wofz as w
...
def dwdq(...):
...
def s(t,E0,sigma_t):
    return -E0*t*np.exp(-0.5*t*t/sigma_t/sigma_t)
def r(t,R0,f0,gamma):
    if(t>=0):
        result = R0*np.cos(2*np.pi*f0*t)
        result *= np.exp(-2*np.pi*gamma*t)
        return result
    else:
        return 0
def math_conv(t,E0,R0,sigma_t,f0,gamma):
    J = complex(0,1)
    units = R0*E0*sigma_t*sigma_t
    x = t/(sigma_t*np.sqrt(2))
    z = (2*np.pi*J*f0-2*np.pi*gamma)
    z *= np.sqrt(2)*sigma_t
    q = -J*(x+0.5*z)
    Re_wq = np.real(w(q))
    Re_dwdx = np.real(-J*dwdq(q))
    result = x*np.exp(-x*x)*Re_wq
    result -= 0.5*np.exp(-x*x)*Re_dwdx
    if(np.isinf(result) or np.isnan(result)):
        return 0.0
    else:
        return -np.sqrt(np.pi)*units*result
```

[1] The IceCube Collaboration, Science **342**, 1242856 (2013), ISSN 0036-8075, 1311.5238.
[2] The IceCube Collaboration, Physical Review Letters **111**, 021103 (2013), ISSN 0031-9007, 1304.5356.
[3] The IceCube Collaboration, The Astrophysical Journal **833**, 3 (2016), ISSN 0004-637X, 1607.08006.
[4] The IceCube Collaboration, Science **361**, 147 (2018), ISSN 0036-8075, 1807.08794.
[5] The IceCube Collaboration, Nature **591**, 220 (2021), ISSN 0028-0836, 2110.15051.
[6] The IceCube Collaboration, Science **378**, 538 (2022), ISSN 0036-8075.
[7] The IceCube Collaboration, Science **380**, 1338 (2023), ISSN 0036-8075.
[8] The KM3NeT Collaboration, Nature **638**, 376 (2025), ISSN 0028-0836.
[9] The IceCube Collaboration, Physical Review D **98**, 062003 (2018), ISSN 2470-0010, 1807.01820.
[10] The IceCube-Gen2 Collaboration, arXiv (2020), 2008.04323.
[11] J. C. Hanson and R. Hartig, Phys. Rev. D **105**, 123019 (2022), URL https://link.aps.org/doi/10.1103/PhysRevD.105.123019.
[12] J. C. Hanson and A. L. Connolly, Astroparticle Physics **91**, 75 (2017), ISSN 0927-6505.
[13] J. Alvarez-Muniz, P. M. Hansen, A. Romero-Wolf, and E. Zas, Phys. Rev. D **101**, 083005 (2020), URL https://link.aps.org/doi/10.1103/PhysRevD.101.083005.
[14] J. C. Hanson et al, Astroparticle Physics **62**, 139 (2015), ISSN 0927-6505, 1406.0820.
[15] J. C. Hanson et al, Journal of Glaciology **61**, 438 (2015), ISSN 0022-1430.
[16] J. Avva, J. Kovac, C. Miki, D. Saltzberg, and A. Vieregg, Journal of Glaciology (2014), 1409.5413.
[17] D. Saltzberg, P. Gorham, D. Walz, C. Field, R. Iverson, A. Odian, G. Resch, P. Schoessow, and D. Williams, Physical review letters **86**, 2802 (2001), ISSN 0031-9007.
[18] P. Miocinovic, R. Field, P. Gorham, E. Guillian, R. Milincic, D. Saltzberg, D. Walz, and D. Williams, Physical Review D **74**, 043002 (2006), ISSN 2470-0029, hep-ex/0602043.
[19] P. W. Gorham, S. W. Barwick, J. J. Beatty, D. Z. Besson, W. R. Binns, C. Chen, P. Chen, J. M. Clem, A. Connolly, P. F. Dowkontt, et al. (ANITA Collaboration), Phys. Rev. Lett. **99**, 171101 (2007), URL https://link.aps.org/doi/10.1103/PhysRevLett.99.171101.
[20] C. Glaser et al, The European Physical Journal C **80**, 77 (2020), ISSN 1434-6044, 1906.01670.
[21] The ARIANNA Collaboration, Journal of Cosmology and Astroparticle Physics **2018** (2018).
[22] The ARA Collaboration, Astroparticle Physics **108**, 63 (2019), ISSN 0927-6505, URL https://www.sciencedirect.com/science/article/pii/S0927650518301154.
[23] The ARIANNA Collaboration, Journal of Instrumentation **15**, P09039 (2020), 2006.03027.

[24] C. Deaconu, A. G. Vieregg, S. A. Wissel, J. Bowen, S. Chipman, A. Gupta, C. Miki, R. J. Nichol, and D. Saltzberg, Physical Review D **98**, 043010 (2018), ISSN 2470-0010, 1805.12576.

[25] C. Welling and T. R.-G. Collaboration, The Cryosphere **18**, 3433 (2024).

[26] R. V. Buniy and J. P. Ralston, Physical Review D **65** (2001), ISSN 2470-0029.

[27] E. Zas, F. Halzen, and T. Stanev, Physical Review D **45**, 362 (1992).

[28] DLMF, *NIST Digital Library of Mathematical Functions*, http://dlmf.nist.gov/, Release 1.1.1 of 2021-03-15, f. W. J. Olver, A. B. Olde Daalhuis, D. W. Lozier, B. I. Schneider, R. F. Boisvert, C. W. Clark, B. R. Miller, B. V. Saunders, H. S. Cohl, and M. A. McClain, eds., URL `http://dlmf.nist.gov/`.

[29] G. B. Rybicki, Computers in Physics **3**, 85 (1989), ISSN 0894-1866.

[30] I. Kravchenko et al, Physical Review D **85**, 062004 (2012), ISSN 2470-0029, 1106.1164.

[31] The ARA Collaboration, Physical Review D **102**, 043021 (2020), ISSN 2470-0010, 1912.00987.

[32] P. Allison, J. Auffenberg, R. Bard, J. Beatty, D. Besson, S. Böser, C. Chen, P. Chen, A. Connolly, and J. Davies, Astroparticle Physics **35**, 457 (2012), ISSN 0927-6505, 1105.2854.

[33] The ARA Collaboration, Journal of Instrumentation **16**, P03025 (2021), 2010.12279.

[34] J. Alvarez-Muniz, A. Romero-Wolf, and E. Zas, Physical Review D **84**, 103003 (2011), ISSN 2470-0029, 1106.6283.

[35] S. Barwick, D. Besson, P. Gorham, and D. Saltzberg, Journal of Glaciology **51**, 231–238 (2005).

[36] The ARIANNA Collaboration, Journal of Cosmology and Astroparticle Physics **2020**, 053 (2020), 1909.00840.

[37] P. Allison, S. Archambault, J. J. Beatty, D. Z. Besson, A. Bishop, C. C. Chen, C. H. Chen, P. Chen, Y. C. Chen, B. A. Clark, et al., Physical Review D **105**, 122006 (2022), ISSN 2470-0010, 2202.07080.

[38] S. Agarwal, J. A. Aguilar, N. Alden, S. Ali, P. Allison, M. Betts, D. Besson, A. Bishop, O. Botner, S. Bouma, et al., arXiv (2024), 2411.12922.

[39] A. Anker, S. Barwick, H. Bernhoff, D. Besson, N. Bingefors, D. García-Fernández, G. Gaswint, C. Glaser, A. Hallgren, J. Hanson, et al., Journal of Cosmology and Astroparticle Physics **2019**, 030 (2019), 1909.02677.